RSC Advances

PAPER

View Article Online
View Journal | View Issue

Cite this: *RSC Adv.*, 2025, **15**, 44356

Self-assembling peptide nanofibers as growth factor-mimicking scaffolds enhancing the bone regeneration potential of nanoceramics: a triad of *in vitro*, *in vivo*, and clinical trial studies

Niloofar Alahdad,[a] Mohammad Ali Yazdanpanah,[a] Mobina Amiri,[a] Mina Iranparvar Alamdari,[bc] Ahad Khoshzaban,[d] Arman Torabizadeh,[e] Seyed Mahdi Rezayat[fg] and Shima Tavakol *[hi]

Nano-tissue engineering utilizing self-assembling peptide nanofibers (SAPNs) offers a groundbreaking approach for repairing critical bone defects, overcoming the osteoinductive, angiogenic, and immunomodulatory limitations of traditional ceramic-based grafts. This study integrates *in vitro*, *in vivo*, and clinical trial evaluations to assess the bone regeneration potential of SAPNs combined with nanoceramics (nHA/TCP). FESEM revealed the structural characteristics of the SAPN (15–20 nm) and the distinct morphologies of nanoHA and β-TCP particles. *In vitro* results revealed the enhanced viability of MSCs and higher matrix mineralization and collagen production in the SAPN-nHA/TCP group compared to those in the nano-HA/TCP group. An *in vivo* study on critical-size bone defects in rats confirmed complete bone regeneration within 75 days in the SPAN nanoHA/TCP group, as evidenced by radiographic and histological evaluations. Gene expression analysis demonstrated the upregulation of osteogenic markers, including alkaline phosphatase, osteocalcin and BMP2. Conversely, the nHA/TCP group exhibited elevated Col1a1 expression, indicating ongoing connective tissue formation, reflecting a less mature stage of bone development relative to the fully ossified state observed in the SAPN-nHA/TCP group. Notably, a clinical trial involving socket preservation (IRCT20210526051407N2) demonstrated significant bone regeneration by 3.5 months post-implantation, with promising bone volume and density metrics. It underscores the real-world applicability of this approach in clinical settings, offering a highly effective solution for the restoration of bone defects that may not otherwise respond adequately to existing bone graft substitutes. These findings highlight SAPN's potential to enhance the bioactivity and osteogenic capacity of nanoceramic scaffolds, advancing bone tissue engineering for critical defect repair.

Received 15th August 2025
Accepted 15th October 2025

DOI: 10.1039/d5ra06036b

rsc.li/rsc-advances

1. Introduction

Recent advancements in nanotechnology have positioned nanotissue engineering as a pivotal approach for the development of efficient biocompatible scaffolds and drug delivery systems aimed at bone regeneration. Researchers in this domain are focusing on innovative therapeutic strategies to enhance bone healing processes.

Bone constitutes a true nanocomposite, comprising both nano-organic and nanoceramic components. To design an effective scaffold, it is paramount to account for both the mineral and organic phases at the nanoscale. Bone defects, which may arise from trauma, infections, inflammation, tumors, or chronic diseases, can impose significant physical and psychological burdens on patients. When the dimensions of a bone defect surpass the critical threshold of approximately 2 cm, complications such as nonunion, malunion, or

[a]*Department of Cell and Molecular Biology, Faculty of Biological Science, Kharazmi University, Tehran, Iran*
[b]*Department of Oral and Maxillofacial Radiology, School of Dentistry, Shahid Beheshti University of Medical Sciences, Tehran, Iran*
[c]*Dental Research Center, Research Institute of Dental Sciences, School of Dentistry, Shahid Beheshti University of Medical Sciences, Tehran, Iran*
[d]*Nano Departement of Eye Translational Research Center, Farabi Eye Hospital, Tehran University of Medical Sciences, Tehran, Iran*
[e]*Oral and Maxillofacial Surgeon, Private Practice, Tehran, Iran*
[f]*Department of Pharmacology, School of Medicine, Tehran University of Medical Sciences, Tehran, Iran*
[g]*Department of Nanomedicine, School of Advanced Technologies in Medicine, Tehran University of Medical Sciences, Tehran, Iran*
[h]*Cellular and Molecular Research Center, Iran University of Medical Sciences, Tehran, Iran*
[i]*Research and Development Department, Tavakol BioMimetic Technologies Company, Tehran, Iran. E-mail: shima.tavakol@yahoo.com*

pathological fractures may occur, necessitating medical intervention.[1,2] The reconstruction of critical bone defects is notably challenging, particularly when they are situated deep within the body and possess irregular geometries.[3] The repercussions of bone fractures extend beyond individual health, leading to absenteeism, diminished productivity, disability, impaired quality of life, and elevated healthcare costs. A meta-analysis encompassing 113 studies estimated the average hospital expenditure for hip fracture treatment at USD 10 075, with cumulative health and social care costs reaching an average of USD 43 669 within one year.[4]

Bone grafts and alloplastic materials serve as substitutes for the repair of such fractures. While autografts are regarded as the gold standard in treatment, allografts and xenografts are also utilized for bone regeneration. Each method has inherent limitations, including donor site morbidity, graft rejection, and suboptimal bone formation, all of which are contingent upon the patient's overall health.[5] The FDA database, along with data from Japan's Drug and Medical Device Agency and Korea's Ministry of Health and Welfare, indicates that 133 alloplastic graft products have received approval.[6] Hydroxyapatite ceramics represent a primary component of bone; in biomedical applications, hydroxyapatite (HA; $Ca_{10}(PO_4)_6(OH)_2$) and tricalcium phosphate (TCP; $Ca_3(PO_4)_2$) are the most prevalent calcium–phosphate-based materials.

Nano-hydroxyapatites (nHA) are distinguished biomaterials for applications in bone substitution, dentistry, and maxillofacial surgery due to their biocompatibility, bioactivity, and osteoconductive potential.[7] The biocompatibility and regenerative efficacy of nHA are influenced by its size and morphology; for instance, plate and needle shapes exhibit greater toxicity than spherical nHA.[8,9] Given that nHA properties closely resemble those of natural HA, they enhance cell adhesion, proliferation, and alkaline phosphatase (ALP) synthesis in osteoblasts, thereby facilitating expedited repair of hard tissue damage.[10–13] However, challenges such as slow degradation rates and cellular calcium influx, along with their crystalline forms, may provoke adverse responses in mesenchymal stem cells (MSCs), prolonging the biodegradability of calcium–phosphate substitutes.[14] To mitigate these issues, β-TCP, which resorbs more rapidly than HA and is recognized as a biodegradable material conducive to bone regeneration, is frequently combined with nHA.[15] Its osteoconductive properties render it suitable for the complete reconstruction of damaged bones.[16] From 1996 to December 2020, a total of 87 alloplastic bone graft products were approved by the FDA, including 15 HA, 21 β-TCP, and 18 biphasic calcium phosphate (BCP), among others. In Japan, 10 alloplastic products (3 HA, 4 β-TCP, one BCP, 1 CA, and 1 OCP) were approved from 2004 to December 2020, while 36 (4 HA, 8 β-TCP, and 15 BCP) were approved in Korea from 1980 to December 2020.[6] While this analysis spans the period up to late 2020, it provides the most recent comprehensive regulatory benchmark available to illustrate the market's focus on non-self-assembling peptide nanofiber-based organic components.

Despite significant developments in bone alloplastic products, only two nanoceramic products currently exist globally: NanoBone® (plate-shaped nHA and silica gel matrix; Artoss GmbH, Warnemünde, Germany, 50 nm)[17] and NMImETIC® Swelling NanoBone Powder™ (less than 50 nm spherical nHA plus TCP). However, both present limitations similar to other ceramics. It is pertinent to note that while MBCP® (Biomatlante, France; nHA/TCP 60/40, approximately 300 nm) and Blue Bone® (Curitiba, Brazil; nHA/TCP 80/20, 130–300 nm) are commercially presented as nanoproducts, their predominant particle sizes, ranging from 130 nm to 300 nm, do not strictly conform to the established nanoscale criteria (*i.e.*, typically below 100 nm). A common challenge faced by all ceramics, including nanoceramics and mineralized grafts from allografts and xenografts, is the lack of growth factors and essential biomolecules that facilitate bone regeneration. To address these limitations, researchers are integrating specific molecules that enhance the regenerative response of bone, thereby overcoming the deficiencies associated with traditional grafting materials.[18]

In recent years, there has been a marked expansion in the field of bone tissue engineering, particularly concerning biomolecules such as peptides. Bioactive peptides, which are short amino acid sequences derived from active protein regions, play a crucial role in modulating biological and physiological processes, regulating cellular activities, and facilitating intercellular communication. The primary sources of these peptides include extracellular matrix proteins (*e.g.*, collagen, fibronectin, bone sialoprotein, and laminin), soluble growth factors, and both engineered and naturally occurring peptides.[19–21] Many peptides exhibit functionality akin to their parent proteins, activating signaling pathways through their interaction with specific cell receptors. Additionally, peptides may be employed to modify biomaterials to enhance their regenerative properties.[22] It is noteworthy that various bioactive peptides have demonstrated significant potential for promoting bone formation both *in vitro* and *in vivo*, with some achieving clinical applications in tissue engineering.[23] Numerous peptides have been developed as candidates to upregulate bone healing responses.[24] Among the extensively researched peptides, considerable attention has been directed toward self-assembling peptide nanofibers, which are seen as promising candidates for bone regeneration due to their nanotopography that simulates the extracellular matrix of bone, as well as their capacity to incorporate biological motifs to further enhance their regenerative potential, rendering them highly suitable for therapeutic applications. Additionally, these peptides can recreate the physiological environment of the body by forming an extracellular matrix characterized by high pore interconnectivity.[25] An early investigation by Zhang *et al.*[26] highlighted the efficacy of peptides as hydrogel materials, which are typically characterized by high biocompatibility and biodegradability, allowing for metabolic assimilation through degradation into amino acids.[27] Misawa *et al.*[28] demonstrated the application of a RADA16 peptide hydrogel in filling calvarial bone defects in mice, marketed as Puramatrix™. Purastat™ is another clinical product derived from this peptide, utilized as a hemostatic agent for injury treatment. Furthermore, Tsukamoto *et al.*[29] illustrated the capacity of an SPG-178-Gel peptide

hydrogel to promote bone regeneration in rats with cranial defects. Tavakol *et al.* explored the attachment of the BMHP1 motif to RADA and KSL cores of self-assembling nanofibers, revealing that both the alteration of biological motifs and the nature of the self-assembling core significantly influence the bone regeneration potential.[30,31]

A comprehensive understanding of how biomaterials interact with cellular signaling pathways is essential for evaluating their biocompatibility and regenerative potential. In this context, the present nanocomposite represents a globally pioneering product. It is distinguished by its unique combination of osteogenic, angiogenic, and immunomodulatory self-assembling peptide nanofibers (US patent: US10485895B2) and nanoceramics (spherical nHA/TCP). Thus, this material stands as the world's first bone alloplastic, showcasing a pivotal synergy between its mineral and organic phases at the nanoscale. In light of these findings and the recognized importance of biological factors and growth factors in the incorporation of nanoceramics, this study investigates two groups: self-assembling peptide nanofibers plus nanoceramics and nanoceramics alone. The synthesis of nHA/TCP composite bioceramic was conducted. These ceramics selected to leverage the beneficial properties of both constituent phases, aiming for a balance between the higher bioactivity of nHA and the enhanced resorbability of TCP. This investigation delves into the bone regeneration efficacy of a novel hybrid biomaterial system. The system comprises osteogenic, angiogenic and immune-modulatory self-assembling peptide nanofibers (peptide nanofiber), incorporating the RADA motif as the organic phase, intricately blended with a mineral phase consisting of spherical nHA and TCP, and it was correlated with the NMImETIC® NanoBone™ product. The regulatory biocompatibility data for this nanocomposite, including all necessary ISO 10993 standard tests for bone grafts mandated by the FDA, are fully reported in our prior publication.[32] The study meticulously compares the bone regeneration capacity of this hybrid construct with that of conventional nanoceramics through a rigorous evaluation encompassing both *in vitro* and *in vivo* experimental paradigms. Furthermore, to assess the clinical translatability of the self-assembling peptide nanofiber construct, the research extends its scope to encompass a human clinical trial model focused on socket preservation. This clinical investigation aims to provide crucial insights into the potential of this innovative biomaterial system for successful bone regeneration in a clinically relevant setting.

2. Experimental

2.1. Synthesis of spherical nHA and TCP powders

Spherical nHA and TCP powders were synthesized by a wet chemical precipitation technique from aqueous solutions. First, stoichiometric quantities of calcium hydroxide [$Ca(OH)_2$] and orthophosphoric acid (H_3PO_4) were employed as precursors for the nHA component.[32,33] These reactants were precisely measured and subsequently combined under rigorously controlled conditions of temperature and pH = 10 to induce the precipitation of nano-hydroxyapatite. Concurrently, tricalcium phosphate (TCP) was prepared separately. This involved the precise stoichiometric combination of calcium hydroxide [$Ca(OH)_2$] and orthophosphoric acid (H_3PO_4), followed by a controlled calcination process to yield the desired TCP phase.

Subsequent characterization of the synthesized materials was performed by X-ray diffraction (XRD) and field emission scanning electron microscopy (FESEM) analyses.

2.1.1. XRD. The crystalline phase compositions of the nHA and TCP powders were rigorously examined by XRD analysis. Diffraction patterns were acquired using an Equinox 3000 diffractometer (INEL, France) operating at 40 kV and 30 mA, with Cu-Kα radiation (λ = 1.5405 Å). Qualitative phase identification was conducted by scanning over a 2θ range of 20° to 45° at a scan rate of 2° min^{-1}.

2.1.2. FESEM. Morphological characterization and particle size determination of the self-assembling peptide nanofibers and synthesized nHA and TCP powders were conducted by FESEM analysis (TESCAN, MIRA 3, USA). Self-assembling peptide nanofibers were mixed with deionized water at a concentration of 1 μg mL^{-1} and imaging was conducted at a voltage of 7 kV. Prior to ceramic imaging, the powder samples were subjected to a sputter coating process, depositing a thin layer of gold (Au) using an Emitech K450X sputter coater (England). Subsequently, the morphology of the gold-coated samples was observed using a FESEM analysis (TESCAN, MIRA 3, USA). This metallization process served to enhance the electron conductivity of the samples, mitigating the charging effects and optimizing the image quality during FESEM analysis.

2.1.3. nHA-TCP extraction. The nHA-TCP extract was prepared by incubating 2 mg mL^{-1} of nHA-TCP powder in PBS at 37 °C for 48 hours under constant agitation (100 rpm). Following the incubation period, the mixture was centrifuged, and the supernatant containing the extracted components was collected. PBS was chosen as the solvent instead of cell culture media to preclude potential interference with the biodegradation and dissolution processes of the calcium–phosphate component. Cell culture media contain a complex mixture of ions, which, according to Le Chatelier's principle, could shift the equilibrium of the dissolution reaction and affect the accurate assessment of the material's behavior. Moreover, it may produce the formation of toxic complexes between the ions and ingredients present in the cell culture media and the biodegraded ceramic components. Using PBS provides a simplified and controlled environment, minimizing the influence of extraneous ions and allowing for a more precise evaluation of the intrinsic biodegradation and dissolution kinetics of the calcium–phosphate material.

2.2. *In vitro* study

Rat mesenchymal stem cells (rMSCs) were harvested from bone marrow aspirates and subsequently expanded *in vitro*. Following two passages, the rMSCs were subjected to treatment with various experimental groups: (1) nHA-TCP nanocomposite extract, (2) nHA-TCP nanocomposite extract supplemented with self-assembling peptide nanofibers, and (3) a control group

(PBS). A volume of 2 μL of the nHA-TCP extract was added to each well of a 96-well plate, a concentration determined based on prior cell viability assays. The self-assembling peptide nanofibers were introduced at a final concentration of 10 μg mL^{-1} in the designated treatment group.

2.2.1. Cell viability using the MTT assay. The cell viability of rMSCs treated with nHA-TCP extract and nHA-TCP extract supplemented with self-assembling peptide nanofibers was assessed using the MTT (3-(4,5-dimethylthiazol-2-yl)-2,5-diphenyltetrazolium bromide) assay. Initially, rMSCs (1×10^4 cells at passage 2) were seeded in a 96-well plate and cultured in a DMEM-F12 medium supplemented with 10% fetal bovine serum (FBS) (AnaCell, Iran) and 1% penicillin/streptomycin (BIO-IDEA, Iran). Cells were maintained at 37 °C in a humidified atmosphere of 5% CO_2 and 95% air for 24 hours. Following this initial incubation period, the culture medium was aspirated and replaced with a fresh medium containing the respective treatment formulations and control group for 48 h. Then, the medium was removed, and the cells were incubated with 100 μL of MTT solution (0.5 mg mL^{-1} in phosphate-buffered saline (PBS)) for 4 hours. Afterwards, 100 μL of dimethyl sulfoxide (DMSO) (Sigma, USA) was added to each well to solubilize the formazan crystals produced by metabolically active cells. The absorbance of the resulting solution was measured at 570 nm using a microplate reader (Bio-Tech) within 20 minutes, and the background absorbance was subtracted. Due to the potential for the self-assembling peptide nanofibers to adsorb the MTT dye and generate false-negative results, background absorbance readings were taken from wells containing nanofibers without cells. All experiments were performed in triplicate, and the results are presented as normalized mean ± standard deviation (SD) of three independent experiments.

2.2.2. Cell membrane damage assay. The potential for cell membrane damage induced by the experimental treatments was assessed by quantifying the release of lactate dehydrogenase (LDH) into the surrounding culture medium. rMSCs (1×10^4 cells at passage 2) were seeded in a 96-well plate and cultured in a DMEM-F12 medium supplemented with 10% fetal bovine serum (FBS) (AnaCell, Iran) and 1% penicillin/streptomycin (BIO-IDEA, Iran). Cells were maintained at 37 °C in a humidified atmosphere of 5% CO_2 and 95% air for 24 h to facilitate cell attachment. Following this initial incubation, the culture medium was removed and replaced with a fresh medium containing the respective treatment formulations (nHA-TCP extract, nHA-TCP extract plus self-assembling peptide nanofibers, or control group) for a 48 h exposure period. LDH release was subsequently quantified using an LDH ELISA kit (KIAZIST, Iran). After the 48 h treatment period, 100 μL of cell culture supernatant from each well was transferred to a corresponding well in a new 96-well plate and mixed with 100 μL of the reaction mixture provided in the ELISA kit. The plate was then incubated for 30 minutes at room temperature in dark. The absorbance was measured at 490 nm using an ELISA reader (Bioteck). LDH release analysis was performed in triplicate, and the results are presented as normalized mean ± standard deviation (SD) of three independent experiments.

2.2.3. NO production. Nitric oxide (NO) production, a marker indicative of both osteotoxicity and osteogenesis, was evaluated. rMSCs (1×10^4 cells at passage 2) were seeded in a 96-well plate and cultured in DMEM-F12 medium supplemented with 10% fetal bovine serum (FBS) (AnaCell, Iran) and 1% penicillin/streptomycin (BIO-IDEA, Iran). Cells were maintained at 37 °C in a humidified atmosphere of 5% CO_2 and 95% air for 24 h to allow for cell attachment. Following this initial incubation, the culture medium was removed and replaced with a fresh medium containing the respective treatment formulations (nHA-TCP extract, nHA-TCP extract plus self-assembling peptide nanofibers, or control medium) for 48 h. Subsequently, 100 μL of cell culture supernatant was transferred from each well to a corresponding well in a new 96-well plate. An equal volume (100 μL) of NO detection dye (Cib Biotech Co., Iran) was added to each well containing the supernatant. Nitrite concentration, representing total NO production, was determined by measuring the absorbance at 570 nm using a microplate reader (Bioteck). The assay was performed in triplicate, and the results are presented as normalized mean ± standard deviation (SD) of three independent experiments.

2.2.4. Calcium deposition analysis using Alizarin red staining. Alizarin red S (ARS) staining was employed to quantify calcium deposition, a marker of osteogenic differentiation, in the treated rMSCs. rMSCs (2×10^4 cells at passage 2) were seeded in a 48-well plate and cultured in a DMEM-F12 medium supplemented with 10% fetal bovine serum (FBS) (AnaCell, Iran) and 1% penicillin/streptomycin (BIO-IDEA, Iran). Cells were maintained at 37 °C in a humidified atmosphere of 5% CO_2 and 95% air for 24 hours to allow for attachment. Following this initial incubation, the culture medium was aspirated and replaced with an osteogenic differentiation medium (NMIm-mETIC Osteogenic Medium minus, Iran). The cells were then treated with the respective experimental formulations, including nHA-TCP extract, nHA-TCP extract plus self-assembling peptide nanofibers, or control medium, for a period of 21 days. The differentiation medium was added every 5 days. The osteogenic differentiation medium was not completely replaced during the 21 day culture period. This approach was adopted to preserve essential factors secreted by the cells that contribute to their osteogenic differentiation. Complete media changes would remove these secreted biofactors, potentially hindering the differentiation process. Therefore, to maintain an optimal environment for osteogenic differentiation while providing fresh nutrients, one-third of the spent medium was removed and replaced with one-half volume of fresh osteogenic medium at each media change (every 4 days). This strategy allowed for the retention of secreted bioactive molecules while replenishing depleted nutrients and maintaining optimal culture conditions.

To mitigate the potential for false-positive staining arising from non-apatitic mineralization and dystrophic mineralization associated with high concentrations of β-glycerophosphate, a modified osteogenic medium of NMImETIC® Osteogenic Medium *Minus* containing a reduced β-glycerophosphate concentration was utilized.[34,35] After the 21 day differentiation

period, the cells were fixed with 70% ethanol for 30 minutes. Following fixation, ARS stain (NMImETIC® Alizarin Red, Iran) was added to each well, and the cells were incubated for 5 minutes. The wells were then carefully washed with PBS to remove unbound stain. The images of the stained cells were acquired using an inverted microscope (Olympus AX-800) equipped with a digital camera (Leica DC200).

2.2.5. Collagen analysis using sirius red staining. Collagen production by differentiating osteoblast-like cells was assessed using sirius red staining.[36] rMSCs (2×10^4 cells at passage 2) were seeded in a 48-well plate and cultured in a DMEM-F12 medium supplemented with 10% fetal bovine serum (FBS) (AnaCell, Iran) and 1% penicillin/streptomycin (BIO-IDEA, Iran). Cells were maintained at 37 °C in a humidified atmosphere of 5% CO_2 and 95% air for 24 h to facilitate cell attachment. After this initial incubation, the culture medium was aspirated and replaced with an osteogenic differentiation medium (NMImETIC® Osteogenic Medium, Iran). The cells were then treated with the respective experimental formulations: nHA-TCP extract, nHA-TCP extract plus self-assembling peptide nanofibers, or control medium for 21 days. A fresh differentiation medium was added every 5 days. On day 21, the culture medium was removed, and the cells were fixed with Kahle's solution, containing 26% ethanol, 3.7% formaldehyde, and 2% glacial acetic acid, 15 minutes at room temperature, followed by rinsing with PBS. Subsequently, 50 μL of Sirius Red dye dissolved in 1% acetic acid (NMImETIC® Sirius Red) was added to each well, and the plates were incubated for one hour at room temperature. Each well was washed with 0.1% HCl, and then, images were acquired using an inverted phase-contrast microscope equipped with a digital camera. For quantitative analysis of collagen content, 100 μL of 0.1% NaOH was added to solubilize the dye bound to collagen. The absorbance of the extracted dye solution was measured at 490 nm. The assay was performed in triplicate, and the results are presented as normalized mean ± standard deviation (SD) of three independent experiments.

2.3. *In vivo* study

2.3.1. Bone defect model in rat. Twelve male Wistar rats (8 weeks old, weighing 200–220 g) were obtained from the Animal Research Center, Pasteur Institute, Tehran, Iran. The animals were housed under standard laboratory conditions with a 12 hour light/dark cycle and provided ad libitum access to food and water. The study received ethical approval form the Iran University of Medical Sciences (IR.IUMS.AEC.1402.004) and adhered to the EU Directive 2010/63/EU guidelines for animal experimentation. The rats were randomly assigned to three experimental groups ($n = 4$ rats including 8 cavities). Group 1 received implants containing 20 mg of nHA-TCP powders; group 2 received 20 mg of nHA-TCP powders plus 10 μL of self-assembling peptide nanofibers; and Group 3 served as the control group, receiving no implants. All surgical procedures were performed under sterile conditions. General anesthesia was induced *via* intraperitoneal injection of a mixture of ketamine hydrochloride (Alfson, Holland) and xylazine (Alfson, Holland) at dosages of 100 mg kg^{-1} and 20 mg kg^{-1}, respectively. The surgical site on the forehead of each rat was shaved and disinfected with povidone-iodine. A longitudinal incision was made along the cranial midline, extending from the nasal bone to the posterior nuchal line, creating a cutaneous flap. A standardized, full-thickness trephine defect, 6 mm in diameter, was created bilaterally in the parietal bone, while carefully preserving the underlying dura mater through continuous irrigation with sterile saline buffer. The defect sites were then covered by repositioning the periosteum and skin, which were subsequently closed using 5–0 vicryl resorbable sutures (Ethicon, Edinburgh, UK). After a 10 weeks implantation period, the general anesthesia was induced prior to cardiac bleeding and subsequent heart removal. The calvarial bone, encompassing the implanted material and surrounding bone tissue, was then carefully dissected and harvested for further analyses.

2.3.2. Radiographic analysis by X-ray. Bone mineral density was assessed *via* radiographic analysis 10 weeks after the surgical procedure. Rats from both the control and intervention groups were euthanized, and their calvaria was harvested. The harvested calvaria was immediately transferred to a cold normal saline buffer, and radiographic imaging was performed. This method allowed for the assessment of bone density without the potential artifacts introduced by fixation. The radiographic images of the rat calvaria were acquired using an X-ray apparatus. The radiographic density and the area of the newly formed bone within the defect sites was then compared between the treatment groups and the control group using the ImageJ software (1.54d, USA). The bone volume (BV) was quantified based on the segmented mineralized voxels within the region of interest (ROI). The final BV/TV ratio, representing the fractional filling of the defect by mineralized tissue, was then calculated for each specimen and plotted.

2.3.3. Alkaline phosphatase (ALP) assay. Serum ALP activity, a marker of osteogenic activity, was measured in the rat serum 75 days post-implantation. An ALP assay kit (PARS AZMUN, Tehran, Iran) was used for the quantification. The absorbance of the reaction product was measured at 405 nm using a microplate reader (Bioteck). The assay was performed in triplicate, and the results are presented as normalized mean ± standard deviation (SD) of three independent experiments.

2.3.4. Gene analysis by qRT-PCR. Seventy-five days after surgery, the rats were anesthetized using a ketamine hydrochloride and xylazine (Alfason) mixture administered intraperitoneally (i.p.) at a dose of 5 mg kg^{-1} body weight for each drug (4/1 ratio of ketamine to xylazine). A 6 mm trephine bur was used to dissect the bone tissue from the defect sites. The harvested bone samples were immediately immersed in an RNX-plus solution and stored at −80 °C to maintain the RNA integrity. The bone sections were homogenized, and total RNA was extracted using an RNX-Plus kit (SinaClon, Iran). Following RNA extraction, the samples were treated with DNase I to remove any contaminating genomic DNA. Complementary DNA (cDNA) was synthesized using random hexamer and oligo-dT primers and a cDNA synthesis kit (FSP Life Sciences, Iran). Real-time quantitative PCR (qPCR) was performed using the synthesized cDNA. A Rotor-Gene Q real-time analyzer (Corbett, Australia) was

employed for the qPCR analysis, running 40 cycles of amplification. The reactions were performed using EVAGreen HRM qPCR Mix 2X (FSP Life Sciences, Iran), and a melting curve analysis was performed after each run to confirm the specificity of the PCR products. Each reaction was performed in duplicate. Relative gene expression levels were determined using the $\Delta\Delta C_t$ method. The β-actin gene served as the internal control for normalization. The primer sequences used for the target genes are listed in Table 1.

2.3.5. Histological analysis. To facilitate histological examination, specimens were initially immersed in a 4% paraformaldehyde solution for fixation (10 days). Subsequently, a decalcification process was employed, whereby specimens were incubated in a 20% ethylenediaminetetraacetic acid (EDTA) solution for a duration of six weeks. Tissue preparation was performed using a tissue processing instrument. Following paraffin embedding, tissue sections of 5 μm thickness were obtained. These sections were subsequently stained with hematoxylin and eosin (H&E) to visualize general tissue morphology. To differentiate between newly formed and mature bone tissue, Masson's trichrome stain was employed. Wright-Giemsa stain was employed to identify infiltrated multinucleated giant cells, a characteristic feature of foreign body response. The stained slides were subsequently mounted with an Entellan mounting medium. The images were captured using an inverted Olympus AX-800 microscope equipped with a Leica DC200 digital camera.

2.4. Statistical analysis

Statistical analysis was performed using the GraphPad Prism software. To compare group means, one-way analysis of variance (ANOVA) was employed for normally distributed data. For non-normally distributed data, the non-parametric Kruskal–Wallis test was utilized. The significance level (α) was predetermined at 0.05, corresponding to a 95% confidence interval (CI). The results were considered statistically significant when the p-value was ≤ 0.05.

3. Results

3.1. Characterization of nHA and β-TCP

An important consideration regarding the imaging of self-assembling peptide nanofibers pertains to the low voltage utilized during imaging, specifically set at 7 kV. Higher voltage levels can lead to the degradation of the peptide nanofibers, preventing the acquisition of clear images. Consequently, optimizing the voltage is critical for effective imaging of self-assembling peptide nanofibers. FESEM analysis related to the self-assembling peptide nanofibers showed nanofibers in the range of 15–20 nm. Moreover, FESEM analysis of ceramics revealed distinct morphological characteristics of the nHA and β-TCP particles (Fig. 1a).[32] nHA particles exhibited a spherical morphology with diameters ranging from 30 to 45 nm. In contrast, β-TCP particles displayed irregular shapes and larger sizes, ranging from 200 to 350 nm. However, these particles were decorated with the TCP nanoparticles in the range of less than 50 nm.

XRD analysis confirmed the chemical structure of the nHA and β-TCP powders. The diffractogram presented in Fig. 1a demonstrates that the characteristic peaks for both samples A (nHA) and B (β-TCP) align with the standard diffraction patterns for hydroxyapatite (reference code 24-0033) and beta-tricalcium phosphate (reference code 01-070-2065), respectively (Fig. 1b).

3.2. *In vitro* results

3.2.1. Cell viability by MTT assay. The cell viability was evaluated using the MTT assay, and statistical significance was determined by one-way ANOVA ($P = 0.0059$). Fig. 2a illustrates that while the nHA-TCP group demonstrated a numerical increase in cell viability compared to the control, this difference was not statistically significant ($P > 0.05$). However, the incorporation of self-assembling peptide nanofibers with nHA-TCP resulted in a substantial and statistically significant enhancement of cell viability compared to both the control ($P < 0.05$) and nHA-TCP alone ($P < 0.01$) (Fig. 2a).

3.2.2. Cell membrane damage assay. LDH release, an indicator of cell membrane damage and cytotoxicity, was measured to assess the potential toxicity of the experimental groups. The results demonstrated that none of the treatment groups induced significant cell membrane damage. Specifically, no statistically significant difference in LDH release was observed between the nHA-TCP group, the nHA-TCP plus self-assembling peptide nanofiber group, and the control group after 48 h of exposure ($P > 0.05$) (Fig. 2b).

3.2.3. NO production. NO concentration, a marker of both potential toxicity and osteogenesis, was measured in the cell culture medium. The results demonstrated that none of the treatment groups induced a significant change in NO

Table 1 The primer sequences of the genes involved in osteogenesis and apoptosis

Gene	Forward primer	Reverse primer
Runx2	5′-CCATAACGGTCTTCACAAATCCT-3′	5′-TCTGTCTGTGCCTTCTTGGTTC-3′
Col1a1	5′-GCTCCTCTTAGGGGCCACT-3′	5′-CCACGTCTCACCATTGGGG-3′
ALP	5′-CAGGGTGGGTTTCTCTCTTG-3′	5′-GAGGGACTGGCTGTGACTATG-3′
OCN	5′-GAGGGCAGTAAGGTGGTGAA-3′	5′-GTCCGCTAGCTCGTCACAAT-3′
BMP2	5′-ACACAGGGACACACCAACCAT-3′	5′-TGTGACCAGCTGTGTTCATCTTG-3′
Bax	5′-CAAGAAGCTGAGCGAGTGTC-3′	5′-TCCACATCAGCAATCATCCTCTG-3′
Bcl2	5′-GGATGACTGAGTACCTGAACCG-3′	5′-TGCACCCAGAGTGATGCAG-3′
β-Actin	5′-CCGCGAGTACAACCTTCTTGC-3′	5′-GTCATCCATGGCGAACTGGTG-3′

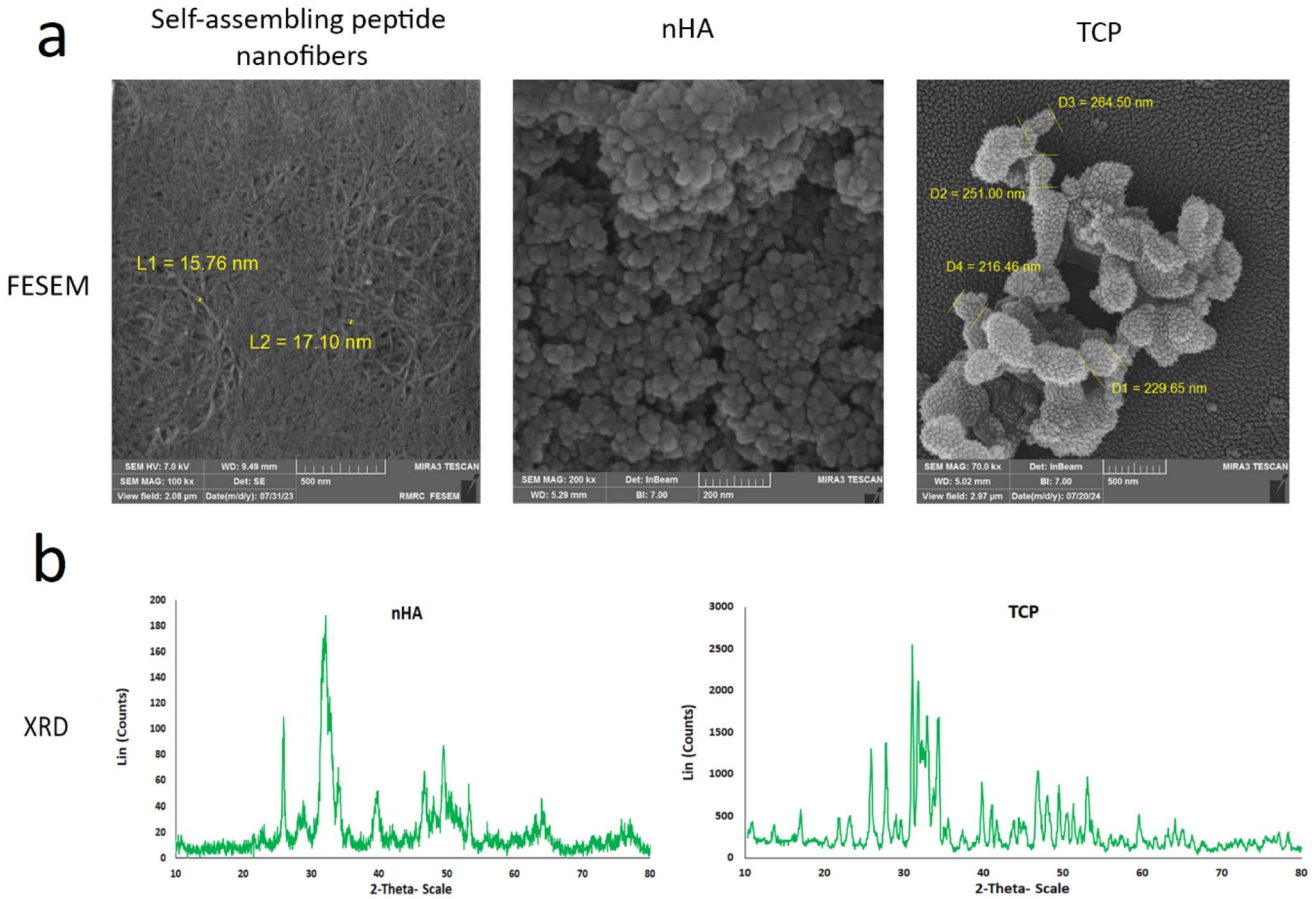

Fig. 1 Characterization of the ceramic powders. (a) Morphological analysis of nHA and TCP was conducted using field emission scanning electron microscopy (FESEM). (b) The chemical structures of nHA and TCP determined *via* X-ray diffraction (XRD). These figures were sourced from http://www.nanomimetic.com/, with all necessary permissions obtained for their reproduction.

production. No statistically significant difference in NO levels was observed between the nHA-TCP group, the nHA-TCP plus self-assembling peptide nanofiber group, and the control group after 48 h of exposure ($P > 0.05$) (Fig. 2c).

3.2.4. Calcium deposition from osteoblast-like cells. Matrix mineralization, a key indicator of osteogenesis, was evaluated using Alizarin Red S (ARS) staining to assess calcium deposition by the differentiated osteoblast-like cells derived from rat stromal cells after 21 days of treatment. As shown in Fig. 3a, the nHA-TCP group plus self-assembling peptide nanofibers exhibited a significantly greater degree of matrix mineralization than that of the nHA-TCP group alone. Furthermore, the nHA-TCP group itself demonstrated significantly enhanced calcium deposition compared to the control group.

3.2.5. Sirius red staining. Collagen production, a crucial aspect of extracellular matrix formation during osteogenesis, was assessed using Sirius Red staining.[36] After 21 days of culture in an osteogenic differentiation medium, the results demonstrated that the nHA-TCP plus self-assembling peptide nanofibers exhibited significantly greater collagen production compared to the nHA-TCP group alone ($P < 0.05$). Moreover, both the nHA-TCP plus self-assembling peptide nanofiber group and the nHA-TCP group showed significantly higher collagen production compared to the control group ($P < 0.01$), as illustrated in Fig. 3b and c.

3.3. *In vivo* study

3.3.1. Bone consolidation by X-ray. X-ray imaging was performed 10 weeks post-operation to assess new bone formation within the critical-size defect. The radiographs revealed increased bone consolidation in the treatment groups compared to the control group. Remarkably, complete bone regeneration within the defect site was observed in the group receiving nHA-TCP plus self-assembling peptide nanofibers. This regeneration was statistically significant compared to both the control group ($P = 0.0002$) and the nHA-TCP group ($P = 0.0008$). Furthermore, the nHA-TCP group demonstrated a statistically significant increase in newly regenerated bone area compared to the control group ($P < 0.001$) (Fig. 4b and c).

3.3.2. Gene expression analysis by qRT-PCR. qRT-PCR analysis, conducted 2.5 months post-implantation, revealed significant differential gene expression profiles among the nHA-TCP plus self-assembling peptide nanofiber, nHA-TCP, and control groups. Specifically, the nHA-TCP plus self-assembling peptide nanofiber group exhibited substantially elevated expression levels of ALP, OCN, and BMP2 genes compared to

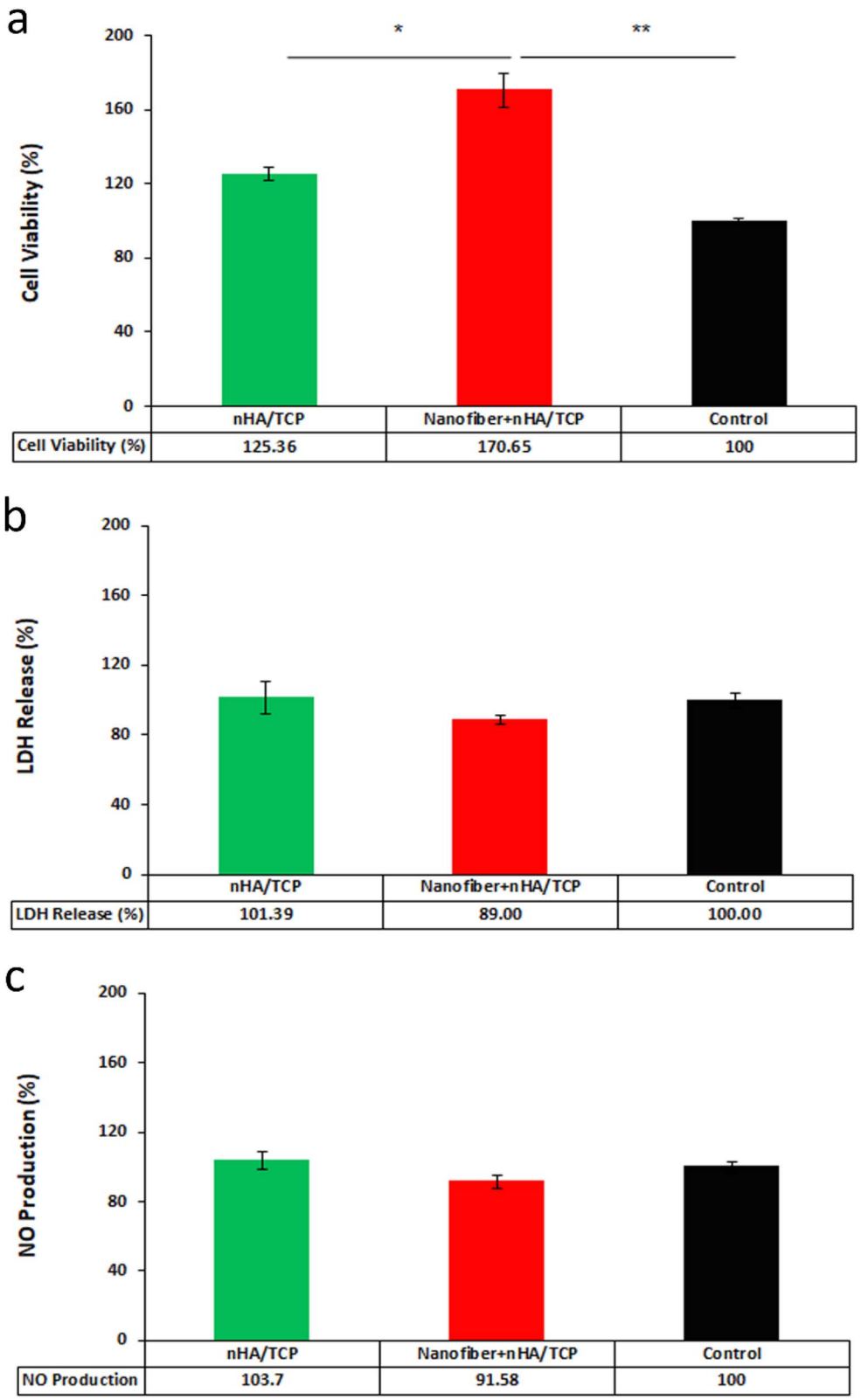

Fig. 2 Cell viability and biocompatibility of the rMSCs. (a) The MTT assay results indicated that the rMSCs treated with the nanofiber + nHA/TCP group exhibited significantly enhanced cell viability compared to those treated with nHA/TCP and control groups after 48 hours. (b) LDH release data demonstrated no significant differences among the rMSCs treated with nanofiber + nHA/TCP, nHA/TCP, and control groups after 48 hours. (c) NO production in rMSCs showed no statistically significant differences across the treatment conditions after 48 hours. Statistical significance is denoted as "***" for $P < 0.001$, "**" for $P < 0.01$, and "*" for $P < 0.05$.

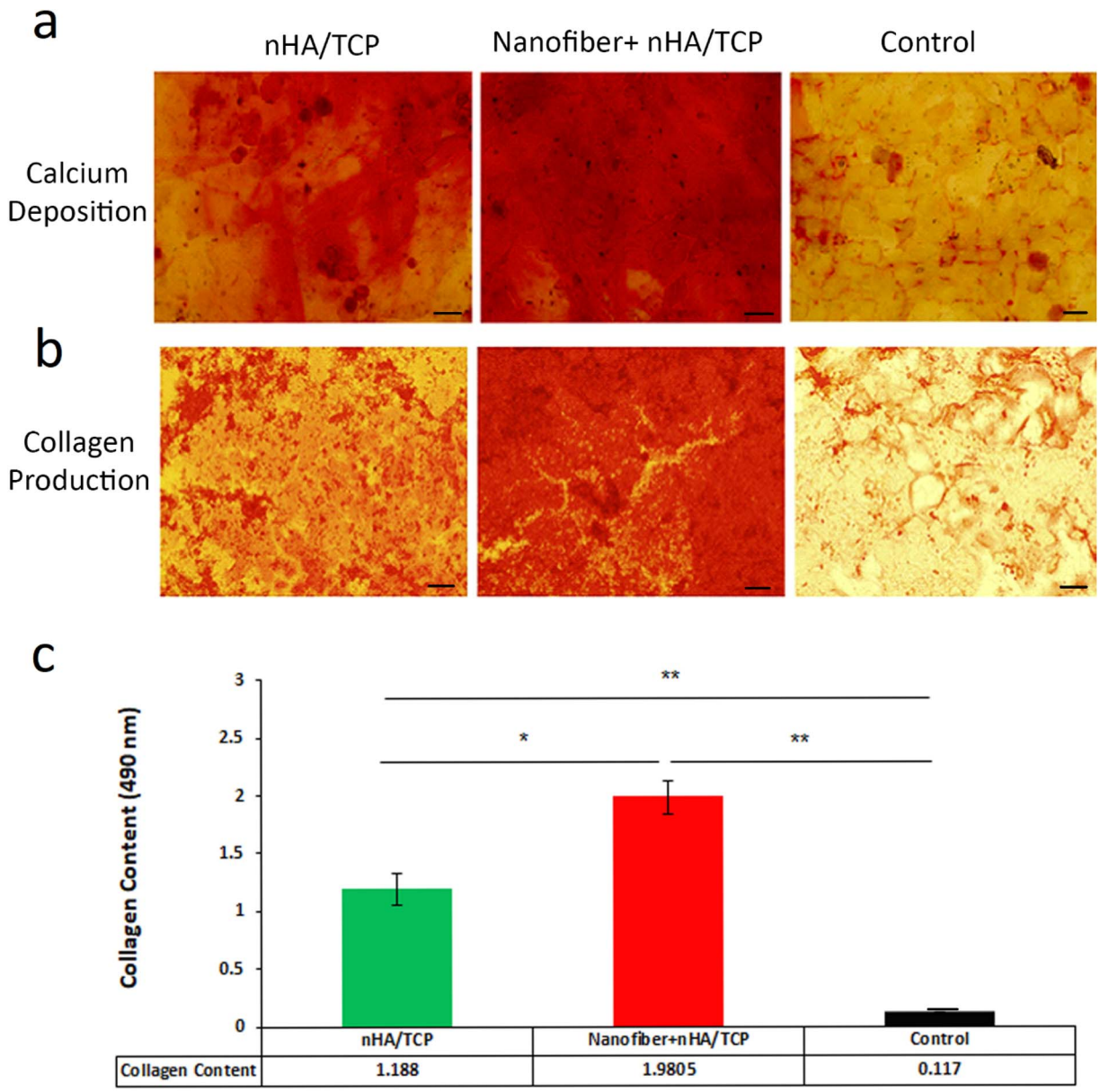

Fig. 3 Calcium and collagen deposition in the rMSCs. (a) Alizarin red staining revealed calcium deposition in the differentiated rMSCs treated with nanofiber + nHA/TCP, nHA/TCP, and control groups after 21 days, indicating greater calcium deposition in the nanofiber + nHA/TCP group. (b) Sirius red staining depicted collagen production in the differentiated rMSCs treated with nanofiber + nHA/TCP, nHA/TCP, and control groups treatments after 21 days. (c) Quantitative analysis of Sirius Red staining confirmed enhanced collagen production in the rMSCs treated with nanofiber + nHA/TCP compared to the other groups after 21 days. Magnification: 20×. Scale bar = 50 μm. Statistical significance is denoted as "***" for $P < 0.001$, "**" for $P < 0.01$, and "*" for $P < 0.05$.

both the nHA-TCP and control groups ($p < 0.05$). While the nHA-TCP group demonstrated significantly increased OCN gene expression relative to the control group ($p < 0.05$), no statistically significant differences in ALP and BMP2 gene expression were observed between the nHA-TCP and control groups ($p > 0.05$). Conversely, the nHA-TCP group displayed significantly higher Runx2 gene expression than that of both the nHA-TCP plus nanofiber group ($p < 0.01$) and the control group ($p < 0.05$). Regarding Col1a1 gene expression, the nHA-TCP group showed significantly elevated levels compared to both the nHA-TCP plus nanofiber group ($p < 0.05$) and the control group ($p < 0.001$). However, the nHA-TCP plus nanofiber group also exhibited significantly higher Col1a1 gene expression than the control group ($p < 0.05$). Analysis of the Bax/Bcl2 ratio revealed no significant difference between the nHA-TCP and control groups ($p > 0.05$). Importantly, the nHA-TCP plus self-assembling peptide nanofiber group demonstrated a significantly reduced Bax/Bcl2 ratio compared to both the nHA-TCP group ($p < 0.05$) and the control group ($p < 0.01$) (Fig. 5a).

3.3.3. ALP activity. Serum alkaline phosphatase (ALP) activity, a marker of osteogenic activity, was evaluated in all three groups after 10 weeks in a rat model of bone defect. While no statistically significant difference in serum ALP activity was observed between the nHA-TCP plus self-assembling peptide

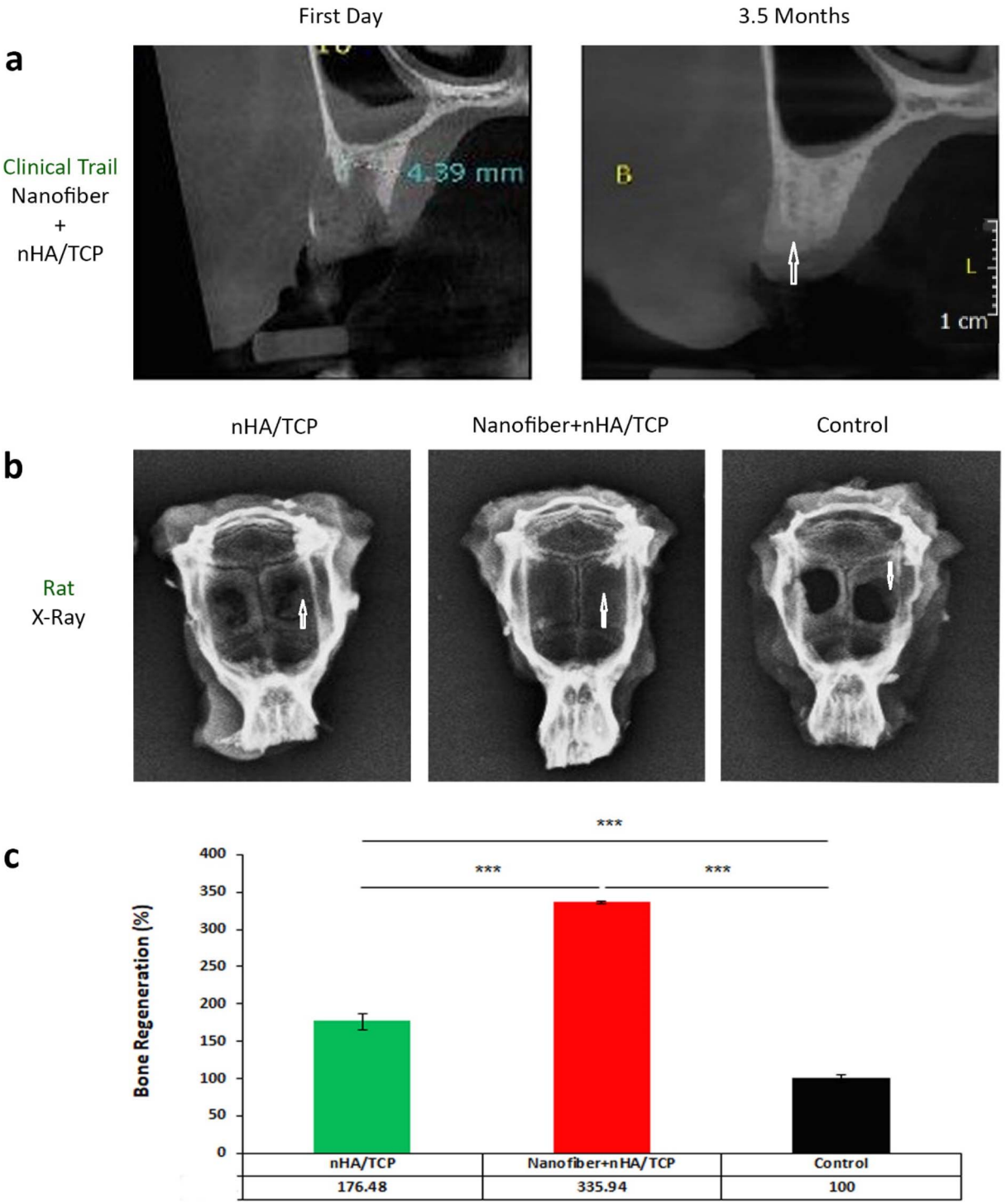

Fig. 4 Clinical trial and radiographic assessment. (a) Cone-beam computed tomography (CBCT) images from patients undergoing socket preservation with nanofiber + nHA/TCP before and 3.5 months post-treatment demonstrated significantly greater bone regeneration at the implant site. Scale bar is 1 cm. (b) X-ray images of rats implanted with nanofiber + nHA/TCP, nHA/TCP, and control groups exhibited notable differences 10 weeks post-implantation. White arrows show new bone formation. Given that these are X-ray images, the known dimensions of the critical-sized defect serve as the inherent internal scale reference. (c) Quantitative analysis of bone regeneration areas in rats revealed complete regeneration of a critical 6 mm defect in the nanofiber + nHA/TCP group after 10 weeks. Statistical significance is denoted as "***" for $P < 0.001$, "**" for $P < 0.01$, and "*" for $P < 0.05$.

nanofiber group and the nHA-TCP group alone ($P > 0.05$), both treatment groups exhibited a significantly higher serum ALP activity than that of the control group ($P < 0.05$) (Fig. 5b).

3.3.4. Histological evaluation by H&E, Masson's trichrome, and Wright-Giemsa staining. Histological analysis was performed to evaluate bone remodeling progression and cellular

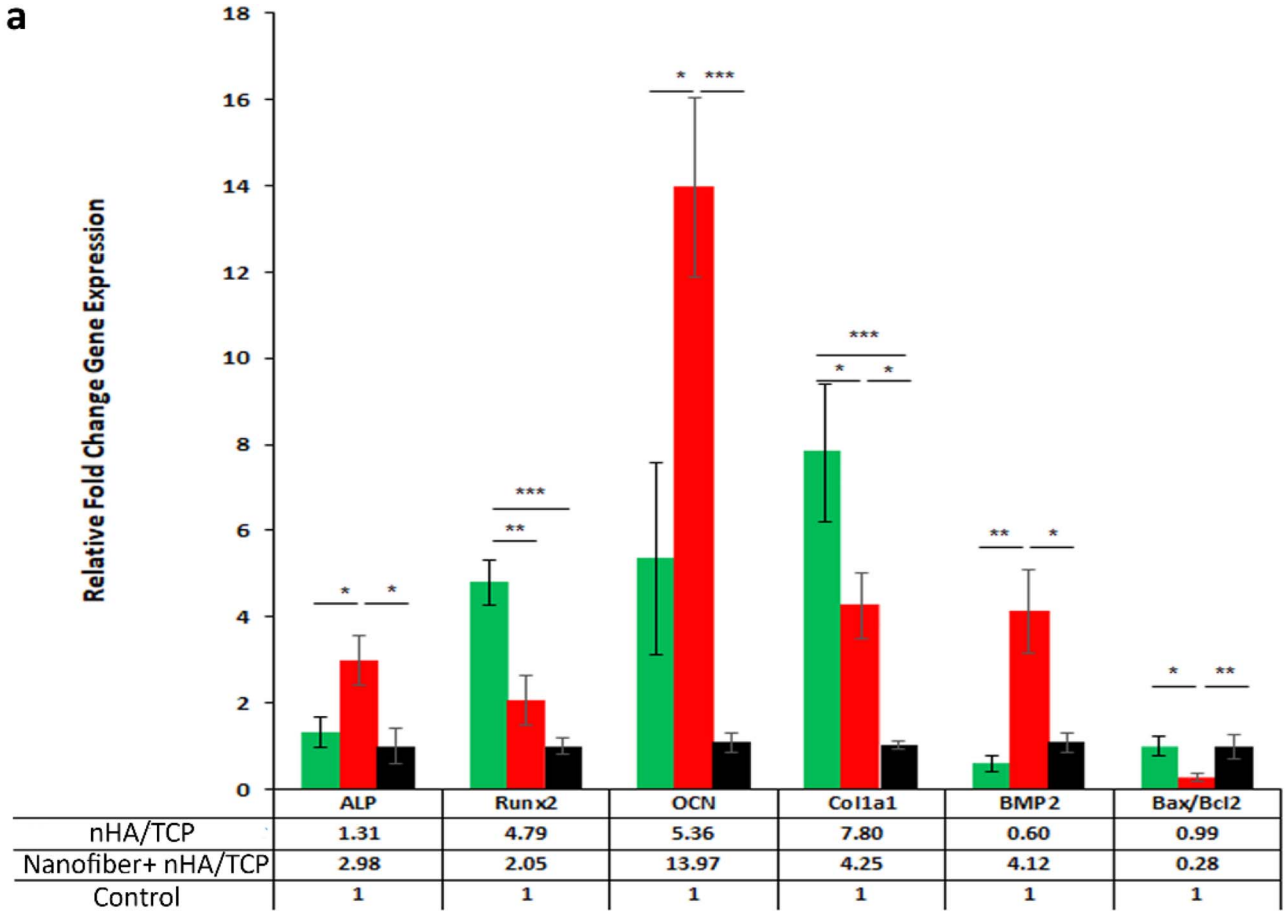

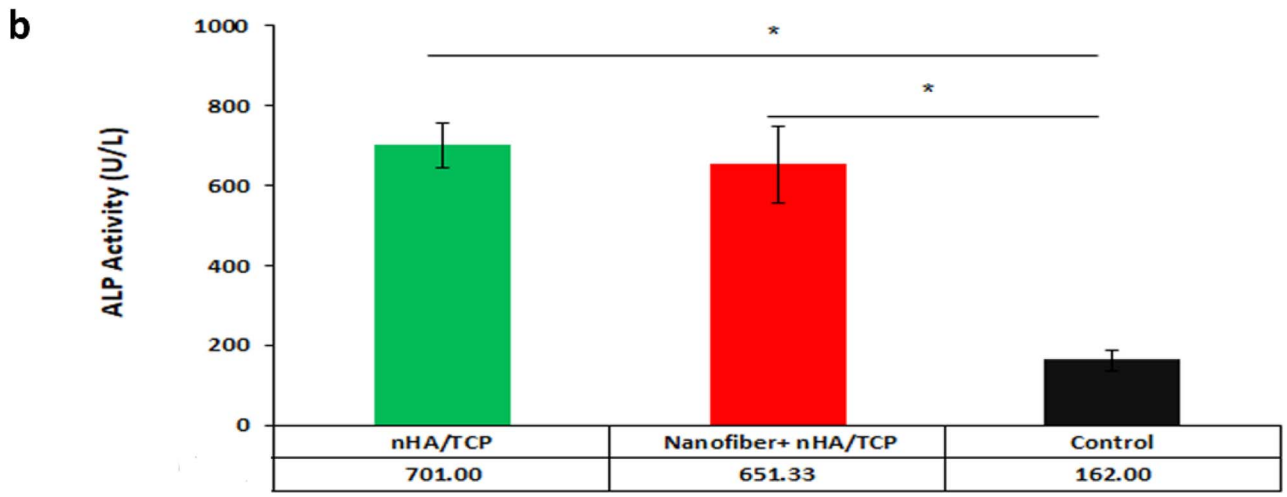

Fig. 5 (a) Gene expression analysis of bone markers. Relative fold changes in gene expression for the osteogenic markers (RUNX2, BMP2, ALP, and OCN) and apoptotic markers (Bax/Bcl2 ratio) were assessed in rats from the control groups and those implanted with nanofiber + nHA/TCP and nHA/TCP after 10 weeks. Data indicated that the implantation of nanofiber + nHA/TCP significantly upregulated osteogenic gene expression and decreased the Bax/Bcl2 ratio compared to the nHA/TCP and control groups. (b) Serum ALP activity in rats implanted with nanofiber + nHA/TCP, nHA/TCP, and control groups was assessed at 10 weeks post-implantation. Statistical significance is denoted as "***" for $P < 0.001$, "**" for $P < 0.01$, and "*" for $P < 0.05$.

events. H&E staining of the nHA-TCP plus self-assembling peptide nanofiber group revealed robust bone formation originating from the center of the defect and extending outwards. Loose connective tissue was replaced by mature bone tissue containing osteocytes, and numerous cavities containing bone marrow and red blood cells were observed. Osteoblasts were

aligned along the margins of the newly formed bone. The nHA-TCP group also demonstrated substantial repair of the tissue defect, with fibrotic tissue being replaced by bone tissue, although to a lesser extent than the nHA-TCP plus nanofiber group. Osteocytes were regularly arranged within lacunae, and bone marrow-containing cavities were present, albeit in lower abundance than the nHA-TCP plus nanofiber group. In contrast, the control group exhibited primarily loose fibrotic connective tissue with minimal bone marrow within the cavities and only small islands of new bone formation at the margins of the defect. Importantly, Wright-Giemsa staining revealed no evidence of polymorphonuclear cells (indicating an absence of significant inflammatory infiltrate) in any of the groups.

Masson's trichrome staining further elucidated the nature of the newly formed bone. In the nHA-TCP plus self-assembling peptide nanofiber group, extensive mature bone tissue (stained red) was observed alongside newly formed bone (stained blue). The nHA-TCP group, while showing new bone formation (blue), exhibited a lesser degree of mature bone. The control group, however, primarily displayed collagen fibers (stained blue) within the defect site, indicating limited bone regeneration. These histological findings corroborate the radiographic observations and further demonstrate the enhanced bone regeneration capacity of nHA-TCP, particularly when combined with self-assembling peptide nanofibers (Fig. 6).

4. Discussion

Nano-tissue engineering offers a transformative approach to addressing critical bone defects, leveraging the inherent nanocomposite structure of natural bone—a complex interplay of nanoscale fibers and ceramics. Traditional bone graft substitutes, often composed solely of ceramics, suffer from limitations in their bone-inductive capacity, resulting in slow and unpredictable new bone formation. However, advancements in tissue engineering open up avenues to enhance these materials. Self-assembling peptide nanofibers have emerged as a promising strategy to augment the osteogenic potential of ceramic-based scaffolds, addressing the deficiency of essential growth factors and biomolecules inherent in purely ceramic materials. This investigation sought to rigorously quantify the augmentation of osteogenic potential conferred by the incorporation of self-assembling peptide nanofibers into ceramic bone graft substitutes and to what degree. To optimize bioactivity, a self-assembling peptide nanofiber was added to nHA/TCP, creating bioactive nanoceramics. *In vitro* studies, using the MTT assay, demonstrated enhanced rMSC viability in the nHA/TCP ceramics plus self-assembling peptide nanofiber group compared to both the nHA/TCP and control groups. While LDH release and NO production showed no significant inter-group differences, the nHA-TCP ceramics plus self-assembling peptide nanofiber group exhibited higher matrix mineralization and collagen production, indicative of enhanced osteogenic differentiation. To further investigate the osteogenesis potency of bone substitutes *in vivo*, they were implanted into a critical-sized bone defect in the rat. Data revealed significantly elevated serum ALP activity in both the nHA/TCP ceramics plus self-assembling peptide nanofiber and nHA-TCP groups compared to the control group, signifying increased osteogenic activity. Radiographic analysis (X-ray) confirmed complete bone regeneration within the defect site in the nHA/TCP plus self-assembling peptide nanofiber group and, to a lesser extent, in the nHA-TCP group, further supporting the efficacy of the self-assembling peptide nanofiber-enhanced scaffold in promoting new bone formation.

A prospective clinical trial was conducted in accordance with the World Medical Association Declaration of Helsinki, which received approval from the Iran University of Medical Sciences' Ethics Committee (TRN: IRCT20210526051407N2) in 2021 in Tehran, Iran. Patients requiring the extraction of premolars and molars were recruited for participation. All individuals underwent screening to meet inclusion and exclusion criteria, and eligible patients were enrolled after confirming their understanding of the study and obtaining a written informed consent ($n = 12$). Self-assembling peptide nanofiber + nHA/TCP were implanted into the extraction sockets, with cone-beam computed tomography (CBCT) performed on the first day and again 3.5 months post-implantation. Subsequently, the bone density and area of regenerated bone were quantified using the ImageJ software. Exploring the potential of this nanocomposite in the clinical trial phase is warranted to translate these promising preclinical findings into clinical applications. Clinical trial study in a model of socket preservation showed significant and robust bone regeneration by 3.5 months post-implantation (bone volume and density of 79.26 ± 6.9 and 77.04 ± 17.11 in the nanocomposite group *versus* -29.3 ± 5.5 and -12.9 ± 5.7 in the untreated group, respectively). Clinical trial results in 12 cases indicated that the nanocomposite—self-assembling peptide nanofibers combined with nHA/TCP—has been successfully conducted in a socket preservation model involving molar and premolar patients (Fig. 4a).[37] The observed expression patterns of ALP, OCN, and BMP2 genes corresponded well with the biocompatibility and calcium/collagen deposition data, with the nHA/TCP plus self-assembling peptide nanofiber group, achieving complete bone repair. Conversely, while Runx2 and Col1a1 gene expression was higher in the nHA-TCP group, the complete bone regeneration observed in the nHA/TCP ceramics plus self-assembling peptide nanofiber group highlights the synergistic benefit of incorporating self-assembling peptide nanofibers.

The enhanced cell viability observed in the nHA/TCP plus self-assembling peptide nanofiber group, as evidenced by MTT assay results and the absence of significant LDH release or NO production indicative of cytotoxicity, can be attributed to a multifaceted interplay of factors. These findings underscore the significant role of self-assembling peptide nanofibers in promoting rMSC viability when combined with nHA-TCP and neither nHA-TCP nor the combination of nHA-TCP with self-assembling peptide nanofibers elicited a cytotoxic response in the rMSCs. It is essential to note that assays utilizing metabolic indicators, such as MTT, quantify the metabolic activity of the cellular population, which is not strictly equivalent to the cell number. The biological mechanism driving this enhanced

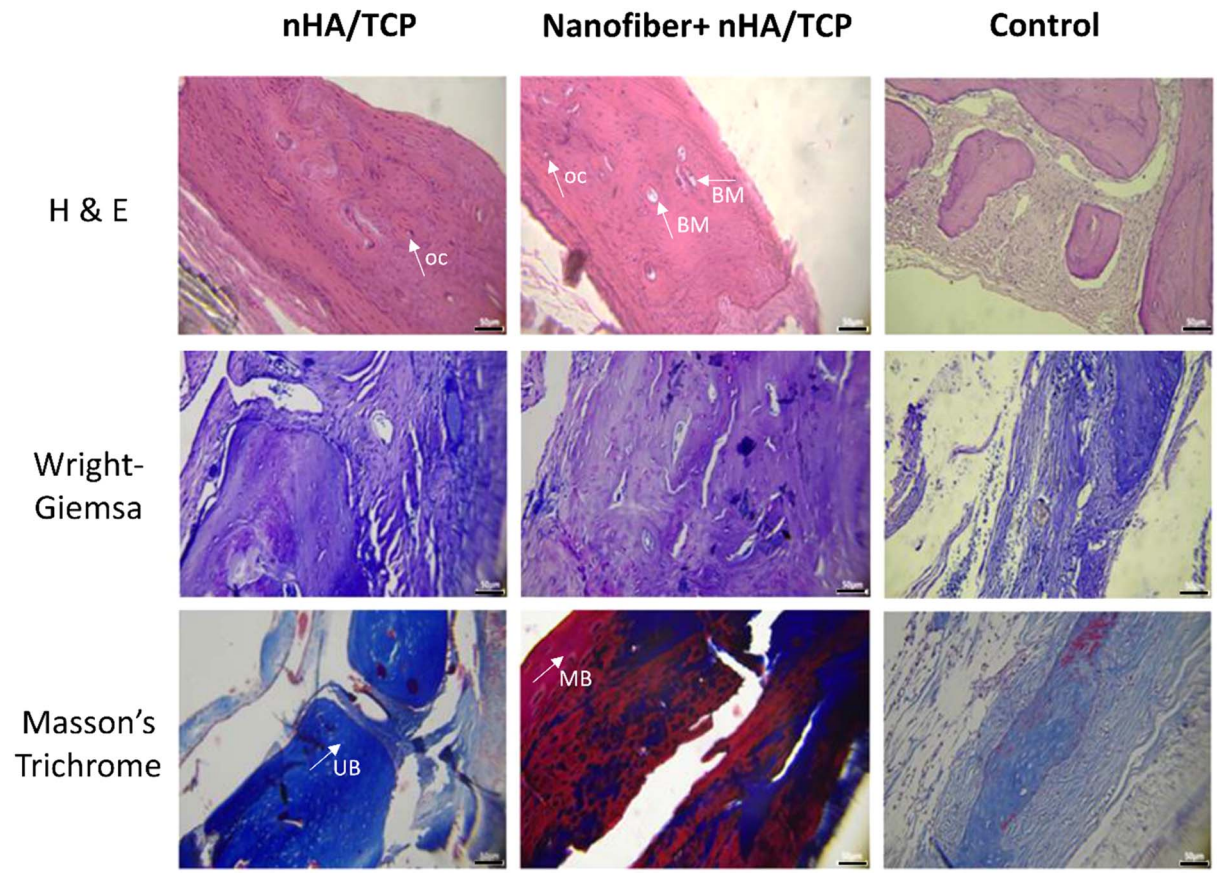

Fig. 6 Histological analysis of bone regeneration. Top to bottom: Hematoxylin and Eosin (H&E), Wright-Giemsa and Masson's trichrome staining of bone defects in rats from the control groups and those implanted with nanofiber + nHA/TCP and nHA/TCP after 10 weeks. The images illustrate significantly enhanced bone regeneration and maturity in the group treated with self-assembling peptide nanofibers, while nHA/TCP exhibited robust regeneration compared to the control group. Magnification: 20×. Scale bar = 50 μm. Bone marrow (BM), osteocyte (OC), mature bone (MB), unmature bone (UB).

viability is supported by the molecular data. The significantly lower Bax/Bcl-2 gene expression ratio in the nHA/TCP + nanofiber group, compared to the control and nHA/TCP groups, indicates that the self-assembling peptide nanofibers actively shift the cellular balance away from apoptosis (programmed cell death). A reduction in apoptosis, coupled with normal proliferation, results in a net increase in the population of living, metabolically active cells on the material. This enhanced cell survival and vitality directly translate to the observed high viability index, thereby promoting the rapid colonization and osteogenesis potential required for successful regeneration. In other words, this performance transcends simple increases in cell proliferation and probably osteo-differentiation; it reflects a profound enhancement of the cellular microenvironment conducive to osteogenesis. The integration of self-assembling peptide nanofibers introduces both bioactive motifs and a unique nanotopographical architecture crucial for effective cell–cell communication, a cornerstone of successful bone remodeling. The nanotopography of the peptide nanofibers plays a pivotal role in mediating cell adhesion and subsequent osteogenic differentiation. Extensive literature supports the critical influence of nanoscale surface features on osteogenesis, from initial cell adhesion to terminal differentiation. For example, self-assembling peptide nanofibers containing either KSL or RADA as a core sequence enhanced the viability of MSCs, although to varying degrees, as indicated by differences in LDH release and NO production.[30,31] This biocompatibility is facilitated by specific nanotopographical cues, and triggers downstream signaling cascades leading to RUNX2 gene expression and osteogenesis. The interaction between integrins and specific peptide sequences within the self-assembling nanofibers initiates signaling pathways, including the activation of focal adhesion kinase (FAK) and protein kinase B (AKT), promoting cell survival and proliferation.[38] These observations were further supported by Wright-Giemsa staining, which confirmed the biocompatibility of both treatment groups and the absence of foreign body reactions or polymorphonuclear cell infiltration at the defect site. This reinforces the conclusion that the intricate interplay between nanotopography and bioactive peptide sequences creates a synergistic effect, optimizing cellular responses.

Furthermore, the high surface area-to-volume ratio inherent in nanofibrous scaffolds, compared to their micrometer-scale counterparts, enhances protein adsorption. This increased

protein adsorption provides a greater abundance of cell recognition sites, promoting robust cell adhesion.[39] The nanotopographical characteristics—fiber diameter and shape—influence protein conformation and epitope availability, potentially triggering signaling cascades such as the mitogen-activated protein kinase (MAPK) pathway, leading to RUNX2 overexpression and enhanced osteogenesis.[40] This phenomenon may be one of the advantages regarding the addition of self-assembling peptide nanofibers and nano HA, as compared to the nHA/TCP alone. This is supported by prior studies demonstrating improved pre-osteoblast adhesion and differentiation on peptide-modified TiO_2 nanotubes[41] and the cytocompatibility and proliferation-promoting effects of RADA16 nanofibers on mesenchymal stem cells (MSCs).[42] The arginine-rich composition of the RADA peptide core is particularly significant, as arginine's positive charge promotes initial cell adhesion through electrostatic interactions with negatively charged cell membranes.[30,43] This enhanced cell adhesion, coupled with the nanofibrous architecture's facilitation of nutrient and waste exchange within a three-dimensional environment, creates an optimal microenvironment for cell growth and differentiation, ultimately contributing to the higher performance observed in the nHA/TCP plus self-assembling peptide nanofiber group.

The biocompatibility of the nHA/TCP plus self-assembling peptide nanofiber construct was further substantiated by molecular analysis of the Bax/Bcl2 gene expression ratio in rat bone. Cellular survival is intrinsically linked to the balance between pro-apoptotic (*e.g.*, Bax) and anti-apoptotic (*e.g.*, Bcl2) proteins. The significant reduction in the Bax/Bcl2 ratio observed in the nHA/TCP plus self-assembling peptide nanofiber group, compared to both the nHA/TCP-only and control groups, strongly suggests a protective effect, promoting cell survival and mitigating apoptosis. This observation is entirely consistent with the enhanced cell viability demonstrated in the *in vitro* MTT assay data, providing robust evidence of the biocompatible and cytoprotective nature of the nanofiber-enhanced scaffold.

Besides biocompatibility, *in vitro* osteogenic analyses revealed a significant enhancement in calcium and collagen deposition, alongside increased OCN gene expression in rat bone tissue, in the nHA/TCP plus self-assembling peptide nanofiber group compared to both the nHA/TCP-only and control groups. These findings align with the improved cell viability and biocompatibility data, strongly suggesting strong ossification potential for the nanofiber-enhanced scaffold. However, a seemingly paradoxical observation emerged, while the nHA/TCP group exhibited a higher fold change in Col1a1 gene expression than that of the nHA/TCP plus self-assembling peptide nanofiber group. This discrepancy between *in vitro* collagen production and *in vivo* Col1a1 gene expression warrants careful consideration. Previous studies have demonstrated the osteogenic potential of self-assembling peptide nanofibers. Tavakol *et al.*[30] reported that RADA-BMHP1 self-assembling peptide nanofibers significantly stimulated calcium deposition and upregulated OCN and Col1a1 gene expression *in vitro*. Furthermore, Rasoulian *et al.*[31] demonstrated that RADA-BMHP1 promoted stronger matrix mineralization and enhanced OCN and Col1a1 gene expression compared to KSL-BMHP1 in osteogenically differentiated mesenchymal stem cells (MSCs). Similarly, surface modification of titanium with osteogenic peptides[62] and cell treatment with SPG-178 self-assembled peptide[29] have been shown to increase matrix mineralization and osteogenic gene expression. The higher Col1a1 expression in the nHA/TCP group *in vivo*, despite the higher mineralization and overall osteogenesis observed in the nHA/TCP plus self-assembling peptide nanofiber group, can be explained by considering the relative proportions of calcified bone tissue *versus* connective tissue. While the nHA/TCP group exhibited a greater extent of bone regeneration and connective tissue formation, this connective tissue, rich in collagen (Col1a1), represented a less mature stage of bone formation than that of the complete ossification observed in the nHA/TCP plus self-assembling peptide nanofiber group. The latter group displayed significantly less connective tissue, indicating a more advanced stage of bone maturation characterized by complete calcification. Therefore, the higher Col1a1 expression in the nHA/TCP group does not necessarily indicate higher bone regeneration; rather, it reflects a greater proportion of unmineralized connective tissue. In summary, the data strongly support the conclusion that the nHA/TCP plus self-assembling peptide nanofiber construct promotes strong bone regeneration (ossification) *in vivo*. The apparent discrepancy regarding Col1a1 gene expression highlights the importance of considering the ratio of calcified bone to connective tissue when interpreting collagen-related data in bone regeneration studies. While connective tissue serves as a crucial substrate and scaffold for subsequent mineralization, complete ossification, as observed in the nHA/TCP plus self-assembling peptide nanofiber group, represents the ultimate goal of bone regeneration. Masson's trichrome staining corroborated these findings, revealing mature bone regeneration (red color) in the nHA/TCP plus self-assembling peptide nanofiber group, whereas the nHA/TCP group exhibited new bone formation with a lesser degree of calcification and a lower proportion of mature bone tissue (blue color). Notwithstanding, the nHA/TCP group, exhibiting greater connective tissue formation than the control group (Col1a1 gene and blue red in Masson's trichrome staining), demonstrates a positive effect, but it remains less effective than the nanofiber-enhanced scaffold in achieving complete bone regeneration. In other words, the observed discrepancy in Col1a1 expression between the nHA/TCP and nHA/TCP plus self-assembling peptide nanofiber groups underscores the importance of considering the relative proportions of mineralized bone *versus* connective tissue when evaluating bone regeneration. While high Col1a1 expression might initially suggest enhanced bone formation, it can also indicate a less mature stage of bone development characterized by a greater abundance of unmineralized collagenous matrix. The complete ossification observed in the nanofiber-enhanced group, in contrast, signifies a more advanced and complete stage of bone regeneration.

Given the critical roles of BMP2, Runx2, and ALP in osteogenic differentiation, their expression levels were evaluated, as

well as in rat bone. BMPs, particularly BMP2, are potent osteoinductive factors that stimulate osteogenesis, in part, by activating Smad1/5 signaling, leading to Runx2 upregulation and subsequent expression of other osteogenic markers, including ALP and OCN.[44] The significant upregulation of BMP2 and ALP gene expression and serum ALP activity observed in the rat bone tissue treated with nHA/TCP plus self-assembling peptide nanofibers suggests that these nanofibers contribute to osteogenesis, at least in part, by enhancing BMP2 expression and potentially exhibiting intrinsic osteoinductive properties. This is strongly supported by the enhanced bone regeneration observed in the nanofiber-containing groups, as evidenced by X-ray radiography and H&E staining, showing increased mineral bone density, organized osteocytes within lacunae, and the presence of bone marrow cavities. The increased BMP2 expression probably leads to increased ALP expression, given ALP's role in mineralization *via* phosphate release.[45] This is consistent with the previous findings demonstrating enhanced ALP activity in MSCs cultured on peptide-modified scaffolds[46] and increased serum ALP activity following implantation of self-assembling peptide nanofibers.[14] Furthermore, the improved cell adhesion and increased bone mineral density observed with the addition of self-assembling peptides to nanohydroxyapatite and chitosan scaffolds further support the beneficial effects of these nanofibers on osteogenesis.[47] Our serum ALP activity findings suggests that both nHA-TCP, with or without the addition of self-assembling peptide nanofibers, stimulated osteogenic activity *in vivo*, although the addition of the nanofibers did not provide a further statistically significant increase in serum ALP activity compared to nHA-TCP alone.

Conversely, the nHA/TCP group exhibited higher Runx2 expression than the nHA/TCP plus self-assembling peptide nanofiber group. The findings about the Runx2 gene are consistent with the temporal dynamics of Runx2 expression during bone regeneration: high initial expression, followed by a decline as ossification progresses and bone regeneration is completed. The complete bone regeneration observed in the nHA/TCP plus self-assembling peptide nanofiber group at 75 days post-implantation accounts for the lower Runx2 expression in this group, reflecting the final stage of bone formation. In contrast, the ongoing, incomplete bone regeneration in the nHA/TCP group is associated with sustained, elevated Runx2 expression, possibly indicating a delay in the ossification cascade compared to the nHA/TCP plus self-assembling peptide nanofiber group. Furthermore, the osteoconductive properties of nHA/TCP resulted in significantly greater bone regeneration than the control group, explaining the higher Runx2 expression (an early osteogenesis marker) in the nHA/TCP group relative to the control.

The optimal SAPN dosage relative to the ceramic mass (nHA/TCP) is highly adaptable and dependent upon the specific clinical requirements of the defect site. This flexibility allows for personalized application based on biological and mechanical needs. For highly necrotic or biologically deficient sites (*e.g.*, poor angiogenesis), a higher volume of SAPN (*e.g.*, 0.9 cc per 0.5 g ceramic) is recommended to maximize the delivery of bioactive signals. Furthermore, a higher SAPN concentration (*e.g.*, 5 mg mL^{-1} instead of the 1 mg mL^{-1} used in this study) is recommended for patients exhibiting low innate angiogenic or osteogenic potential (*e.g.*, elderly or diabetic patients).

For defects requiring higher mechanical load-bearing capacity, a slightly reduced SAPN volume (*e.g.*, 0.7 cc per 0.5 g ceramic) is recommended to maintain the higher relative density and mechanical support provided by the ceramic phase. This adaptive dosing strategy underscores the translational utility of the composite, allowing clinicians to modulate the material's regenerative *versus* mechanical emphasis.

5. Conclusion

In conclusion, this study demonstrates the significant enhancement of bone regeneration achieved by incorporating self-assembling peptide nanofibers into nHA/TCP ceramic bone graft substitutes. *In vitro* analyses revealed higher biocompatibility, matrix mineralization, and collagen production in the nanofiber-enhanced group than the nHA/TCP alone and control groups. *In vivo* studies using a critical-sized rat bone defect model confirmed these findings, demonstrating complete bone regeneration within 75 days in the nHA/TCP plus self-assembling peptide nanofiber group, as evidenced by radiographic analysis and histological staining (H&E and Masson's trichrome). Gene expression analyses revealed upregulation of key osteogenic markers (BMP2, ALP, and OCN) in the nanofiber-enhanced group, further supporting its strong osteogenic potential. While the nHA/TCP group exhibited higher Runx2 and Col1a1 expression, reflecting a greater proportion of unmineralized connective tissue, the complete ossification observed in the nanofiber group highlights the synergistic effect of the nanofibers in promoting mature bone formation. The enhanced bioactivity likely stems from a combined effect of the bioactive peptide sequences and the unique nanotopographical architecture of the nanofibers, optimizing cell–cell communication and promoting cell survival and proliferation *via* various signaling pathways. The elevated performance of the nHA/TCP plus self-assembling peptide nanofiber construct represents a significant advancement in bone tissue engineering, offering a promising strategy for addressing critical bone defects. Future studies could focus on optimizing the peptide sequence and concentration to further enhance osteogenesis and explore the long-term efficacy and biomechanical properties of this novel bone graft substitute. The investigation of the specific signaling pathways activated by the interaction between the peptide nanofibers and osteoprogenitor cells could provide further mechanistic insights into the observed effects. The findings suggest that the nanotopographical cues provided by the self-assembling peptide nanofibers play a crucial role in directing osteogenesis, highlighting the potential of nano-tissue engineering strategies to overcome the limitations of traditional bone graft substitutes. The more efficient performance of the self-assembling peptide nanofiber-enhanced scaffold is not merely the result of increased cell proliferation but also an indication of the profound improvement in the cellular microenvironment inductive to osteogenesis.

Author contributions

N. A., M. A. Y., A. T. and M. A. contributed to investigations. A. K. contributed to investigations and writing and editing. M. I. P. contributed to investigation and formal analysis. S. M. R. contributed to conceptualization and formal analysis. S. T. contributed to conceptualization, data curation, supervision, methodology, investigation, formal analysis and funding acquisition. All the authors commented on the previous versions of the manuscript and contributed to writing. All the authors have read and approved the final manuscript.

Ethical statement

The present study was a prospective, randomized controlled clinical trial performed in accordance with the World Medical Association Declaration of Helsinki and was reviewed and approved by the Institutional Ethics Committee at the Iran University of Medical Sciences (IRCT20210526051407N2).

Conflicts of interest

I declare that the authors have no competing interests that might be perceived to influence the results and/or discussion reported in this paper. Shima Tavakol has an affiliation with the Tavakol BioMimetic Technologies company and is the inventor and assignee of US patent US10485895B2. She received NMImETIC® Sirius Red as a gift.

Data availability

The data generated in the present study may be requested from the corresponding author.

Acknowledgements

We are thankful to the Iran University of Medical Sciences, Tehran, Iran, for supporting this study with grants (grant number: 1401-4-20-25178, 0-1-20-20349, 1403-3-99-31942) and the National Institute for Medical Research and Development, Tehran, Iran, supported this study with a grant (grant number: 4003436). Moreover, we are thankful to Tavakol BioMimetic Technologies company for providing us with NMImETIC® Sirius Red.

References

1 J. F. Keating, A. Simpson and C. Robinson, *J. Bone Jt. Surg., Br.*, 2005, **87**, 142–150.
2 R. T. Annamalai, X. Hong, N. G. Schott, G. Tiruchinapally, B. Levi and J. P. Stegemann, *Biomaterials*, 2019, **208**, 32–44.
3 R. Li, C. Zhou, J. Chen, H. Luo, R. Li, D. Chen, X. Zou and W. Wang, *Bioact. Mater.*, 2022, **18**, 267–283.
4 A.-M. Wu, C. Bisignano, S. L. James, G. G. Abady, A. Abedi, E. Abu-Gharbieh, R. K. Alhassan, V. Alipour, J. Arabloo and M. Asaad, *Lancet Healthy Longev.*, 2021, **2**, e580–e592.
5 D. Xia, F. Yang, Y. Zheng, Y. Liu and Y. Zhou, *Bioact. Mater.*, 2021, **6**, 4186–4208.
6 S. Fukuba, M. Okada, K. Nohara and T. Iwata, *Materials*, 2021, **14**, 1096.
7 S. Tavakol, M. R. Nikpour, E. Hoveizi, B. Tavakol, S. M. Rezayat, M. Adabi, S. Shajari Abokheili and M. Jahanshahi, *J. Nanopart. Res.*, 2014, **16**, 1–13.
8 X. Zhao, S. Ng, B. C. Heng, J. Guo, L. Ma, T. T. Y. Tan, K. W. Ng and S. C. J. Loo, *Arch. Toxicol.*, 2013, **87**, 1037–1052.
9 L.-H. Huang, X.-Y. Sun and J.-M. Ouyang, *Sci. Rep.*, 2019, **9**, 18979.
10 M. Azami, S. Tavakol, A. Samadikuchaksaraei, M. S. Hashjin, N. Baheiraei, M. Kamali and M. R. Nourani, *J. Biomater. Sci., Polym. Ed.*, 2012, **23**, 2353–2368.
11 Y. Cai, Y. Liu, W. Yan, Q. Hu, J. Tao, M. Zhang, Z. Shi and R. Tang, *J. Mater. Chem.*, 2007, **17**, 3780–3787.
12 Z. Shi, X. Huang, Y. Cai, R. Tang and D. Yang, *Acta Biomater.*, 2009, **5**, 338–345.
13 S. Tavakol, I. Ragerdi Kashani, M. Azami, A. Khoshzaban, B. Tavakol, S. Kharrazi, S. Ebrahimi and S. M. Rezayat Sorkhabadi, *J. Nanopart. Res.*, 2012, **14**, 1–14.
14 S. Tavakol, B. Rasoulian, F. Ramezani, E. Hoveizi, B. Tavakol and S. M. Rezayat, *Mater. Sci. Eng., C*, 2019, **101**, 148–158.
15 S.-C. Wu, H.-C. Hsu, S.-K. Hsu, F.-W. Lin and W.-F. Ho, *Ceram. Int.*, 2015, **41**, 7596–7604.
16 M. Bohner, B. L. G. Santoni and N. Döbelin, *Acta Biomater.*, 2020, **113**, 23–41.
17 A. S. Alagl and M. Madi, *J. Int. Med. Res.*, 2018, **46**, 2001–2007.
18 G. Bullock, J. Atkinson, P. Gentile, P. Hatton and C. Miller, *J. Funct. Biomater.*, 2021, **12**, 22.
19 R. Visser, G. A. Rico-Llanos, H. Pulkkinen and J. Becerra, *J. Controlled Release*, 2016, 122–135.
20 M. Berg, G. A. Chasse, E. Deretey, A. Füzéry, B. Fung, D. Fung, H. Henry-Riyad, A. Lin, M. Mak and A. Mantas, *J. Mol. Struct.:THEOCHEM*, 2000, **500**, 5–58.
21 G. A. Chasse, A. M. Rodriguez, M. L. Mak, E. Deretey, A. Perczel, C. P. Sosa, R. D. Enriz and I. G. Csizmadia, *J. Mol. Struct.:THEOCHEM*, 2001, **537**, 319–361.
22 F. R. Maia, P. L. Granja and C. C. Barrias, *Acta Biomater.*, 2013, 8773–8789.
23 M. P. I. Pountos, A. Lampropoulos, E. Jones, G. M. Calori and P. V. Giannoudis, *BMC Med.*, 2016, 103.
24 S. Azadi, M. A. Yazdanpanah, A. Afshari, N. Alahdad, S. Chegeni, A. Angaji, S. M. Rezayat and S. Tavakol, *J. Tissue Eng.*, 2024, **15**, 20417314241303818.
25 N. Marí-Buyé, T. Luque, D. Navajas and C. E. Semino, *Tissue Eng., Part A*, 2013, **19**, 870–881.
26 S. Zhang, T. Holmes, C. Lockshin and A. Rich, *Proc. Natl. Acad. Sci. U. S. A.*, 1993, **90**, 3334–3338.
27 Y. Fan, G. Ren, Y. Cui, H. Liu, S. Li, Y. Tian, G. Wang, C. Peng, Y. Wang and D. Wu, *Mater. Des.*, 2023, **229**, 111862.
28 H. Misawa, N. Kobayashi, A. Soto-Gutierrez, Y. Chen, A. Yoshida, J. D. Rivas-Carrillo, N. Navarro-Alvarez, K. Tanaka, A. Miki and J. Takei, *Cell Transplant.*, 2006, **15**, 903–910.

29 J. Tsukamoto, K. Naruse, Y. Nagai, S. Kan, N. Nakamura, M. Hata, M. Omi, T. Hayashi, T. Kawai and T. Matsubara, *Tissue Eng., Part A*, 2017, **23**, 1394–1402.
30 S. Tavakol, B. Rasoulian, F. Ramezani, E. Hoveizi, B. Tavakol and S. M. Rezayat, *Mater. Sci. Eng., C*, 2019, **101**, 148–158.
31 B. Rasoulian, Z. Sheikholislam, M. H. H. Tehrani, S. Chegeni, E. Hoveizi, S. M. Rezayat and S. Tavakol, *Regener. Ther.*, 2024, **26**, 999–1009.
32 S. Chegeni, H. Tavakol, S. M. Rezayat and S. Tavakol, *Nanotoxicology*, 2025, 1–19.
33 M. Azami, S. Tavakol, A. Samadikuchaksaraei, M. S. Hashjin, N. Baheiraei, M. Kamali and M. R. Nourani, *J. Biomater. Sci., Polym. Ed.*, 2012, **23**, 2353–2368.
34 F. Langenbach and J. Handschel, *Stem Cell Res. Ther.*, 2013, **4**, 1–7.
35 C.-H. Chung, E. E. Golub, E. Forbes, T. Tokuoka and I. M. Shapiro, *Calcif. Tissue Int.*, 1992, **51**, 305–311.
36 C. Szász, D. Pap, B. Szebeni, P. Bokrossy, L. Őrfi, A. J. Szabó, Á. Vannay and A. Veres-Székely, *Int. J. Mol. Sci.*, 2023, **24**, 17435.
37 E. Tahmasebi, S. Azadi, S. Hajisadeghi, H. Barikani, M. Salehi, M. Shafikhani, F. Mozaffari, E. Nazarpour, A. Torabizadeh and A. J. R. T. Khoshzaban, *Nanotoxicology*, 2025, **28**, 134–142.
38 C. G. Gahmberg and M. Grönholm, *Trends Biochem. Sci.*, 2022, **47**, 265–278.
39 C. Hess, A. Schwenke, P. Wagener, S. Franzka, C. Laszlo Sajti, M. Pflaum, B. Wiegmann, A. Haverich and S. Barcikowski, *J. Biomed. Mater. Res., Part A*, 2014, **102**, 1909–1920.
40 Y. Xia, H. Chen, F. Zhang, L. Wang, B. Chen, M. A. Reynolds, J. Ma, A. Schneider, N. Gu and H. H. Xu, *Artif. Cells, Nanomed., Biotechnol.*, 2018, **46**, 423–433.
41 S. Sun, W. Yu, Y. Zhang and F. Zhang, *J. Mater. Sci.: Mater. Med.*, 2013, **24**, 1079–1091.
42 S. Chen, A. Zhou, B. He, W. Zhao, X. Chen and D. Jiang, *Int. J. Mol. Med.*, 2017, **40**, 679–688.
43 K. Ando, S. Imagama, K. Kobayashi, K. Ito, M. Tsushima, M. Morozumi, S. Tanaka, M. Machino, K. Ota and K. Nishida, *PLoS ONE*, 2018, **13**, e0190833.
44 J. Guicheux, J. Lemonnier, C. Ghayor, A. Suzuki, G. Palmer and J. Caverzasio, *J. Bone Miner. Res.*, 2003, **18**, 2060–2068.
45 J. Yang, L. E. McNamara, N. Gadegaard, E. V. Alakpa, K. V. Burgess, R. D. Meek and M. J. Dalby, *ACS Nano*, 2014, **8**, 9941–9953.
46 Z. Qu, J. Yan, B. Li, J. Zhuang and Y. Huang, *Biomed. Mater.*, 2010, **5**, 065001.
47 Z. Zhang, G. Wu, Y. Cao, C. Liu, Y. Jin, Y. Wang, L. Yang, J. Guo and L. Zhu, *Mater. Sci. Eng., C*, 2018, **93**, 445–454.